Materials Today Communications 26 (2021) 101902

Contents lists available at ScienceDirect

Materials Today Communications

journal homepage: www.elsevier.com/locate/mtcomm

Sluggish hydrogen diffusion and hydrogen decreasing stacking fault energy in a high-entropy alloy

Zhoucan Xie [a,b,c], Yunjiang Wang [a,b,c], Chunsheng Lu [d], Lanhong Dai [a,b,c,*]

[a] State Key Laboratory of Nonlinear Mechanics, Institute of Mechanics, Chinese Academy of Sciences, Beijing 100190, PR China
[b] School of Engineering Science, University of Chinese Academy of Sciences, Beijing 101408, PR China
[c] CAS Center for Excellence in Complex System Mechanics, Beijing 100190, PR China
[d] School of Civil and Mechanical Engineering, Curtin University, Perth, WA 6845, Australia

ARTICLE INFO

Keywords:
High entropy alloys
Hydrogen embrittlement
Diffusion barrier
Chemical order
Stacking fault energy

ABSTRACT

Hydrogen diffusion and its interaction with dislocations play an important role in hydrogen embrittlement, however, such a process in multiple-principal high entropy alloys (HEAs) is still elusive. Here, first-principles calculations were performed to investigate the solution and diffusion of hydrogen and its effect on the stacking fault energy of FeCoNiCrMn. It is shown that the unique lattice distortion in HEAs causes a wide distribution of local hydrogen solution energy, and the trapping of hydrogen in low energy sites increases diffusion barriers. The zigzag path and asymmetry of forward and backward diffusion result in the sluggish diffusion of hydrogen. Furthermore, hydrogen reduces unstable and stable stacking fault energies, originated from the transfer of electron between hydrogen and metal atoms, which promotes formation of deformation twins. This provides a theoretical guidance for designing novel engineering materials with optimal combination of their mechanical properties and hydrogen embrittlement resistance.

1. Introduction

Strength, ductility and damage tolerance are several key mechanical properties of metallic materials for developing energy-efficient and lightweight structural components in a wide variety of industries, including energy supply, transportation and infrastructure. Under hydrogen-rich environments, however, sudden fracture that is usually referred to as hydrogen embrittlement occurs in metallic materials, which may cause catastrophic and unpredictable industrial accidents [1–4]. Several mechanisms have been proposed on hydrogen embrittlement of traditional single principal element alloys, such as hydrogen-enhanced decohesion [5–9], hydrogen enhanced localized plasticity [10–13], formation of a hydride phase [14,15] and blister or bubble formation [16]. There is still no consensus on its physical origin, and especially recent researches have shown that chemical composition and atom-packing order play an important role in hydrogen embrittlement [17,18].

High entropy alloys (HEAs) [19–21], a new class of multiple-principal and chemical-disordered alloys, have drawn surging interest due to their superior mechanical properties, such as high cryogenic fracture toughness [22], exceptional combination of strength and ductility [23–30], and excellent impact resistance [31–33]. These superior mechanical properties are mainly derived from the chemical disorder at atomic-level, where diverse elements are randomly arranged on crystallographic positions [34–37]. It is such an inhomogeneous distribution of elements that triggers strong fluctuation of the local stacking fault energy (SFE). Thus, glide of dislocations and formation of twins or new phases simultaneously occur, which leads to increase of strength and ductility. In addition, element segregation and heterogeneity in HEA have been verified by experiments [38–42].

HEAs also possess the promising functional properties related to corrosion and hydrogen embrittlement resistance [43–51], and have a wide potential application under extreme industrial environments. Compared with traditional alloys, instinctive lattice defects and stress fields in HEAs offer abundant low energy sites for the trapping of hydrogen [46,47,52], and hydrogen sluggishly diffuses due to inherent and rugged potential energy surfaces [18,45,47], remarkably retarding long-distance hydrogen migration. On the other hand, the fracture surface of HEAs with hydrogen presents intergranular cleavage and piled dislocation slip bands [53], as well as displays dense twins that impede crack propagation [18,48,49]. That is, aggregation of hydrogen and synergy of multiple plastic deformations play a vital role in hydrogen

* Corresponding author at: State Key Laboratory of Nonlinear Mechanics, Institute of Mechanics, Chinese Academy of Sciences, Beijing 100190, PR China.
E-mail address: lhdai@lnm.imech.ac.cn (L. Dai).

https://doi.org/10.1016/j.mtcomm.2020.101902
Received 4 September 2020; Received in revised form 20 November 2020; Accepted 20 November 2020
Available online 25 November 2020

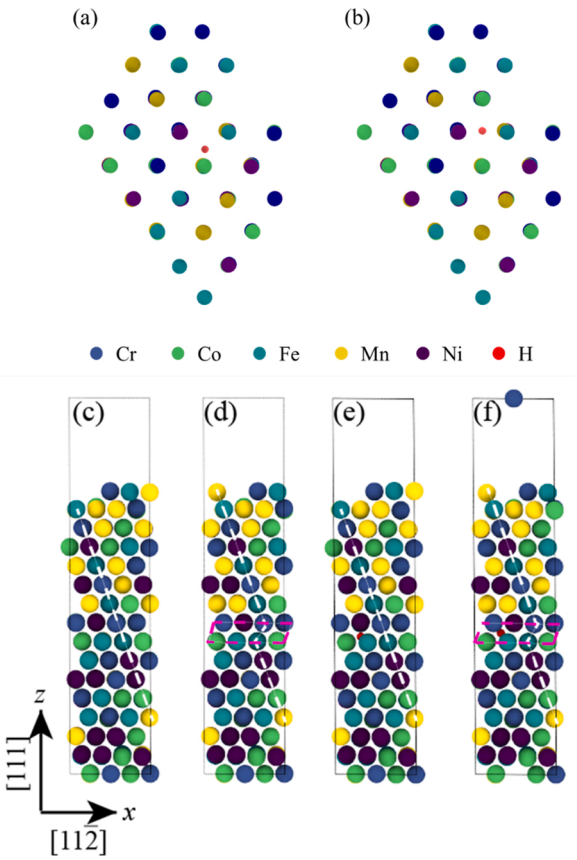

Fig. 1. Configurations with (a) a H tetrahedral interstitial atom, (b) a H octahedral interstitial atom, (c) a prefect crystal, (d) a crystal with SF, (e) a crystal with H and (f) a crystal with SF and H.

embrittlement of HEAs [18]. Under complex chemical environments, however, the atomic-scale transferring behavior of hydrogen and the interaction of hydrogen between defects in HEAs are illusive. Thus, it is necessary to perform a comprehensive study of novel hydrogen embrittlement in HEAs. Here, atomistic and electronic-level simulations have been resorted to analyze hydrogen diffusion and its interaction with dislocations.

The diffusion coefficient and SFE are known to be two critical parameter to describe hydrogen migration and plastic deformations in metals, respectively [17,34,54,55]. In this paper, first-principles calculations are carried out to investigate the solution energy, the diffusion coefficient of hydrogen and effects of chemical order and hydrogen on SFE in FeCoNiCrMn HEA. It is shown that the small diffusion coefficient and the reduction of SFE may provide a deep understanding on the superior hydrogen embrittlement resistance.

2. First-principles calculations

First-principles calculations were performed based on Vienna Ab initio Simulation Package with the projector augmented wave method [56]. In calculations, the plane wave cutoff energy was 420 eV, and the energy and force convergence criterion were set to be 10^{-5} eV and -0.02 eV/Å, respectively. The collinear spin polarization (ISPIN = 2) was enabled. All HEA supercells were generated by using special quasi-random structure method and alloy theoretic automated toolkit codes [57].

HEA supercells with 80 atoms were established and fully relaxed with 4 × 4 × 4 K-points gird, and hydrogen (H) atom was inserted into tetrahedral interstitials (TIs) (Fig. 1(a)) or octahedral interstitials (OIs) (Fig. 1(b)). The solution energy is calculated by: $\Lambda = E_H - E_{ini} - 1/2E_{H_2}$,

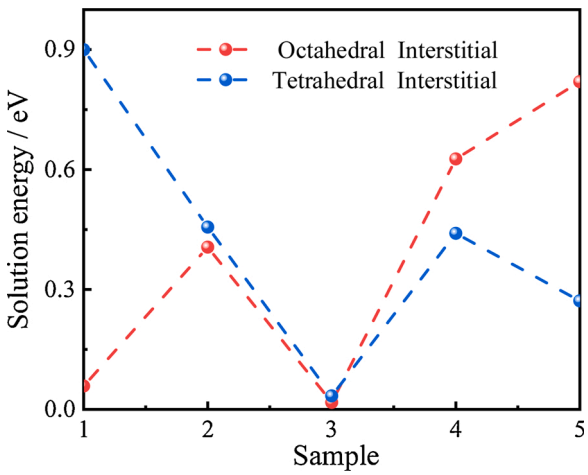

Fig. 2. The solution energy of an H atom in different interstitial sites.

where E_{ini} and E_H are the total energies of relaxed configurations with perfect lattice and the one embedding H atom, respectively, and E_{H_2} is the chemical potential of H_2 in the gas phase. The climbing-image nudged elastic band method [58] was applied to determine the diffusion barrier of H interstitial atom. Two optimized supercells with H interstitial atom were selected as the initial and final configurations, and six intermediate structures were interpolated along a pathway and connected like a "spring band" to search the minimum energy path.

What is more, we built six independent initial supercells, containing 120 atoms and 15 close-packed (111) atomic planes in the z direction (Fig. 1(c)). Here 30 supercells with stacking fault (SF) were created by shifting atoms above five different slip planes along the <112> direction in each initial supercell (Fig. 1(d)). Then, a vacuum layer of 10 Å was added above the periodically repeated slabs, and the bottom and top layers of atoms were fixed. Brillouin zone integrations were performed using Monkhorst-Pack meshes with a 5 × 8 × 1 grid. To obtain the effect of hydrogen on SFE in FeCoNiCrMn, H atom was introduced into the interstice between the sliding atomic layers (Fig. 1(e) and 1(f)). The stacking fault energy γ can be calculated by:

$$\gamma = \frac{E_{SF} - E_{ini}}{A} \quad (1)$$

where E_{SF} and E_{ini} are the total energies of configurations with and without a SF, respectively, and A is the area of SF.

3. Results and discussion

3.1. Hydrogen diffusion in HEAs

In a pure face-centered cubic metal, there are two kinds of interstitial positions due to the periodicity. However, the diversity of chemical environments breaks the high symmetry of lattice in HEAs, and then all TIs or OIs are no longer equivalent. Here, ten random interstitial sites were chosen, including five OIs and TIs, to study the solubility of H atom in FeCoNiCrMn HEAs. Fig. 2 shows that the H solution energy splits into multiple values, rather than a single value in a pure metal or dilute alloy. In addition, OI is slightly superior to TI for H residing as a whole.

Hydrogen diffusion between interstitial positions can be considered as a thermal activation event. According to Einstein's equation, the atomic diffusion coefficient can be written as: $D = \beta L^2 \Gamma$, where β is a coefficient related to the type of interstitial positions, L is the jump length projected onto the diffusion direction, and Γ is the effective atomic jump frequency between neighboring sites. Based on the transition state theory [59], the effective atomic jump frequency can be derived as: $\Gamma = \nu_0 e^{-E_m/k_B T}$, where k_B is the Boltzmann constant, T is temperature, E_m is the diffusion barrier, and the vibration frequency (ν_0)

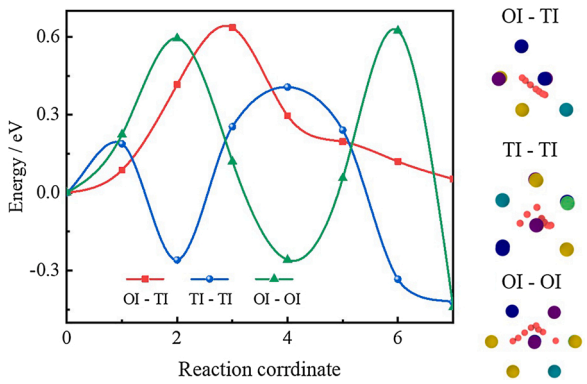

Fig. 3. Hydrogen diffusion pathways in HEAs, where red, blue and green lines represent the diffusion paths of OI–TI, TI–TI and OI–OI, respectively. (For interpretation of the references to colour in this figure legend, the reader is referred to the web version of this article).

is : $\nu_0 = \prod_1^{3N} \nu_i^{ini} / \prod_1^{3N-1} \nu_i^{sad}$, where ν_i^{ini} and ν_i^{sad} are the atomic vibration frequencies of initial stable structure and saddle structure, respectively. Here, the metal atoms were set to be fixed owing to their relatively heavy mass.

The barriers of three typical diffusion paths were calculated: from OI to TI (OI–TI), TI–TI and OI–OI. As shown in Fig. 3, the diffusion barriers (0.17–1.05 eV) vary with local chemical environments and are obviously higher than that in pure metals [33,34]. Interestingly, the diffusion path is not the geometric shortest path for TI–TI and OI–OI and always contains OI–TI or TI–OI. In all situations, the vibration frequencies from OI and TI to transient state are close to 9.9 THz and 30.1 THz, respectively.

Generally speaking, spatial composition variation is inevitable in multiple principal elements. Electronic charge transfer between hydrogen and different metal atoms causes local fluctuation of potential energy surface and thus, the solution energy of hydrogen is variant in HEAs. Such nanoscale heterogeneities may favor H trapping and enhance its solubility in HEAs. That is, hydrogen must overcome a high barrier to escape from local interstitial positions. Furthermore, hydrogen diffuses only along the paths of OI–TI and TI–OI and it cannot directly diffuse between OI–OI and TI–TI, resulting in a zigzag diffusion path. The distinct forward and backward vibration frequencies and diffusion barriers break the periodicity and symmetry of hydrogen diffusion in HEAs. This makes it difficult to predict the next jumping of H atom in HEAs. Thus, the high diffusion barrier, zigzag diffusion path and asymmetry induce sluggish diffusion of hydrogen in HEAs, which impedes hydrogen accumulation at various defects and enhances resistance of hydrogen embrittlement.

3.2. *Influence of hydrogen on SFE*

Compared with the traditional alloys, SFE of HEA is not only determined by distance change between the second nearest neighbor atoms, but also related to local chemical environment in the stacking fault zone. As shown in Fig. 4(a), SFE values of these samples distribute in a wide range and even can be negative. In the low SFE crystals, plasticity is primarily achieved by phase transformation and twins; and for the high SFE, dislocation gliding plays a leading role [37]. Therefore, the wide distribution of SFEs is helpful to the activation of several plastic deformation events in HEAs, which results in an excellent combination of high hardening rate, ultimate strength and tensile ductility. Furthermore, SFE increases with the contents of Mn and Cr, and decreases with the Co contents, but it is basically independent of Fe and Ni. SFE is mainly dependent on valence density count and *d*-electron density [36]. Since Mn, Cr and Co all have valence electrons in *d* orbitals and their bond strengths are high, the content changes of these elements significantly affect their SFE. As reported, the poor Co [36] and rich Cr [34] regions have a higher SFE in CoCrNi. However, Fe and Ni have nearly full *d* shells and weak bond strengths, and their contents make less contribution to SFE.

As shown in Fig. 4(b), no matter samples contain hydrogen or not, SFEs obey normal distribution with average value of -107.07 and -5.43 mJ/m^2 for HEAs with and without hydrogen, respectively. That is, hydrogen reduces stacking fault energy of HEA. Furthermore,

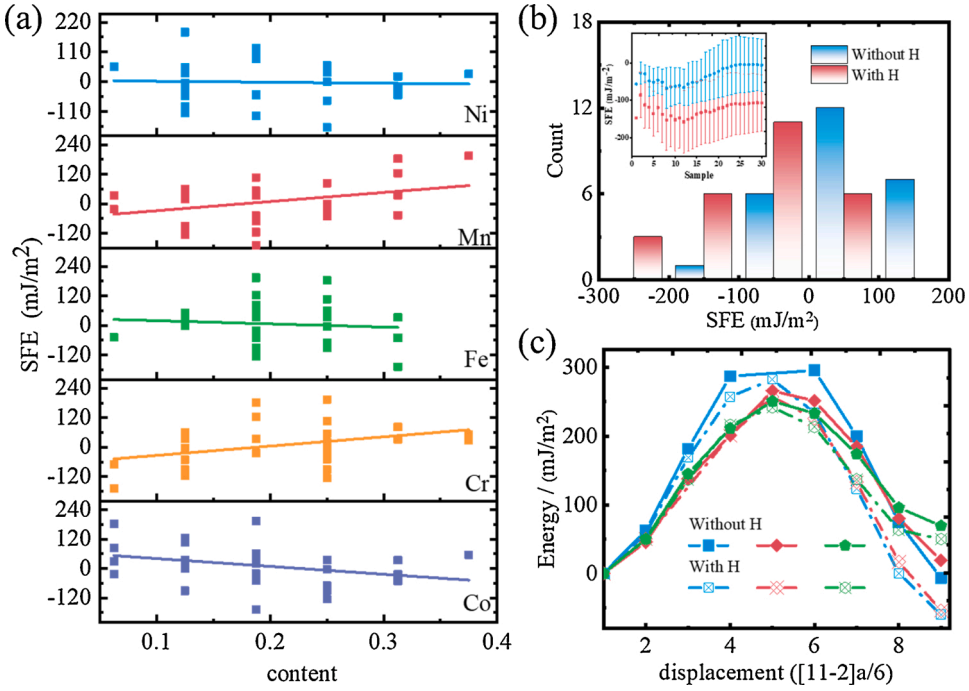

Fig. 4. (a) Effects of the chemical order on SFE, where straight lines represent the linear fitting. (b) The influence of hydrogen on SFE, where inset represents the average SFE and standard deviation with the number of samples. (c) Generalized planar stacking fault energy curves.

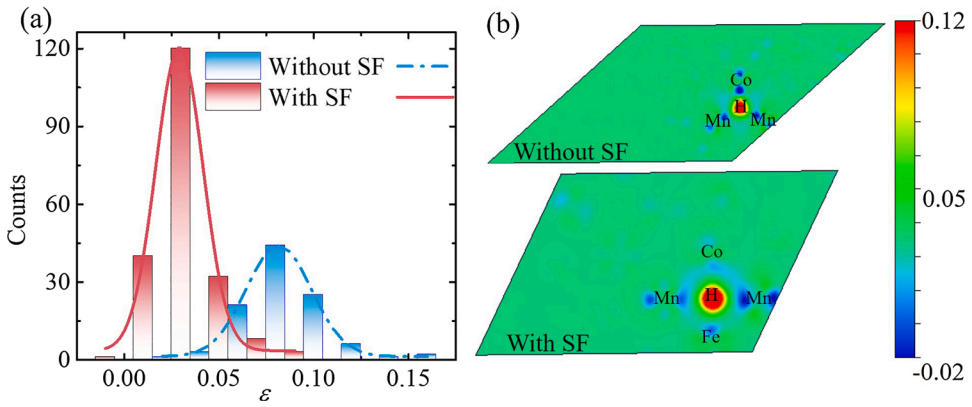

Fig. 5. (a) Effect of hydrogen on the bond strength, where dotted lines represent the normal distribution. (b) Charge density difference between configurations without and with SFEs, respectively. Red and blue colors represent electron gain and depletion, respectively. (For interpretation of the references to colour in this figure legend, the reader is referred to the web version of this article).

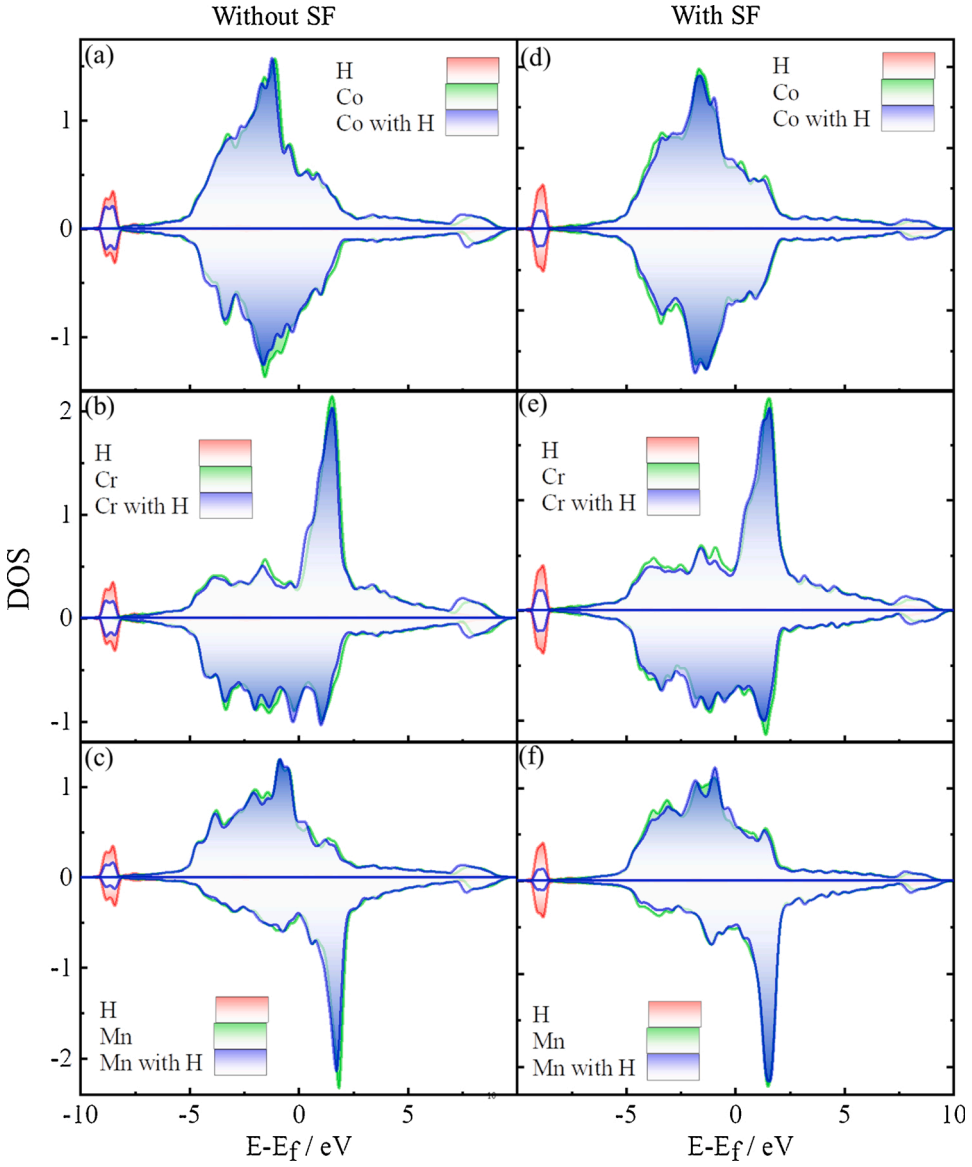

Fig. 6. (a–c) The local density of states of Co, Cr and Mn atoms in initial configurations without and with H atom, respectively. (d–f) The local density of states of Co, Cr and Mn atoms in SF configurations without and with H atoms, respectively.

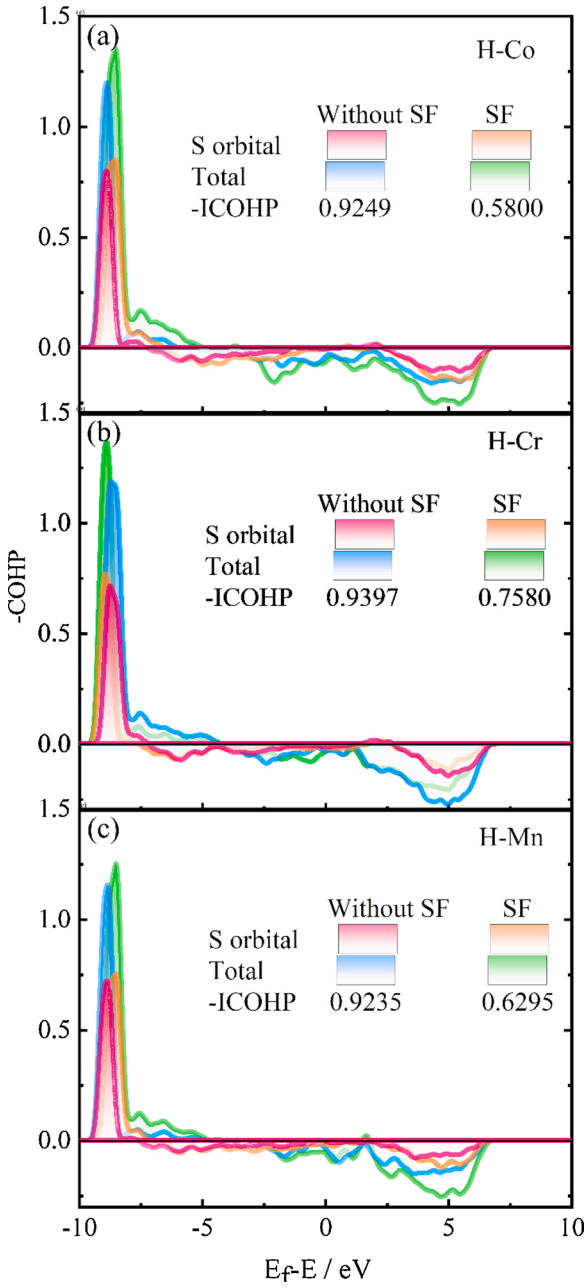

Fig. 7. The COHP between H and (a) Co, (b) Cr and (c) Mn atoms, respectively.

generalized planar stacking fault energy curves were calculated by selecting three configurations (Fig. 4(c)). It is seen that the unstable SFE is positive in all samples. Although the energy of stacking fault configuration is lower than that of initial configuration, there is an energy barrier during formation of stacking faults, and the initial FCC phase is metastable. Hydrogen also reduces the unstable SFE of HEAs, which promotes formation of stacking faults and twins. In other words, hydrogen promotes a significant production of nano-twins during deformation, which increases increasing the work-hardening capability, strength and ductility.

As is known, primary plastic deformation mechanism in FeCoNiCrMn is due to partial dislocation gliding and twins, and its critical resistance to partial dislocation nucleation is proportional to the unstable SFE [62]. It implies that hydrogen simultaneously reduces the dislocation nucleation stress. Yang [43] confirmed the effect of hydrogen on onset of plastic deformation through analysis of the first pop-in during nanoindentation. This is consistent with description of H-enhanced local plasticity, which is also verified by the morphology of fracture surfaces after tensile testing [48].

Next, influence of H atom was investigated from the viewpoint of bond length and electronic structure. The relative change of bond length between the nearest-neighbor metal atoms of a hydrogen atom can be calculated by: $\varepsilon = \frac{l^{H}_{ini,SF} - l_{ini,SF}}{l_{ini,SF}}$, $l_{ini,SF}$ and $l^{H}_{ini,SF}$ are the metal-metal bond lengths in sample without and with hydrogen, respectively. It is seen from Fig. 5(a) that hydrogen increases the length of a metal-metal bond and a larger relative change occurs in the configuration without stacking faults. Thus, the increase of bond length results in decrease of bond strength. That is, hydrogen weakens the metal-metal bond.

The charge density difference of an H atom in HEA in Fig. 5(b) is calculated by: $\Delta\rho = \rho_{HEA-H} - \rho_{HEA} - \rho_{H}$, where ρ_{HEA-H} represents the electron density of HEA with H atom, and ρ_{HEA} and ρ_{H} represent the electron densities of pure HEA and H atom, respectively. As shown in Fig. 5(b), the charge density around H increases but it decreases around metal atoms. The charge transfers from metal to H atom, and the H atom forms a bond with its nearest metal atoms. However, the charge density in the region between the adjacent metal atoms obviously decreases, implying that the metal-metal bond weakens.

To explore electronic-level bonding properties, the local electronic density of states of hydrogen and its nearest-neighbor metal atoms were calculated. From Fig. 6(a–f), no matter whether samples contain hydrogen or stacking fault, the Fermi level is occupied by electrons, showing characteristics of metals. Compared with local electronic density of states in configurations without hydrogen, metal atoms exhibit a distinct peak around −8 eV in configurations with hydrogen (purple line), and the position matches the peak of H atom (red line), which indicates that orbits of metal atoms hybridize with that of H atom.

A detailed crystal-orbital Hamilton population (COHP) calculation was conducted to describe bonding and antibonding contributions to bond-structure [63]. The integration of COHP (ICOHP) curve up to the Fermi level gives the total overlap population of a bond and it is a measure of the bond strength. It is seen from Fig. 7(a) that -COHP is positive around −8.0 eV and negative around 5.0 eV, indicating that the bond at −8.0 eV is H–Co bonding and the bond at 5.0 eV is H–Co antibonding. Moreover, the major contribution of hybridization is from 1 s orbit of H and 4 s orbit of Co. The bond energies between the H and Co atoms in configurations without SFE and with SFE are 0.9 eV and 0.5 eV, respectively. That is, H and Co can form a stronger bond in the configuration without SFE, resulting in a clearer changes in bond length and charge transfer. The trends of H-Cr and H-Mn bond are similar to that of H–Co (Fig. 7(b) and (c)).

As shown in Fig. 8(a), bond strengths exhibit obvious fluctuation under different local chemical environments, which results in the variety of solution energy. The bond strength of H-Cr (i.e., the average strength of 0.49 and 0.42 eV in configuration without and with SF, respectively) is much larger than that of H and other metal atoms. It is because Cr can offer more valence electrons and form more stable bonds with H. At the same time, the bond strength between nearest-neighbor metal atoms of H atom was calculated (see Fig. 8(b) and (c)). In the initial configuration, the average metallic bond energies without and with hydrogen are 0.57 eV and 0.23 eV, respectively. In SF configuration, the average metallic bond energies without and with hydrogen are 0.45 eV and 0.28 eV, respectively. Hydrogen reduces the metallic bond energy and the weakening effect of H on bond strength is more noticeable in the initial configuration. The charge transfer between metal and H atoms causes the increase of metal-metal bond length and the decease of its bond strength. Therefore, atoms move more easily along the slip plane and there is a lower unstable SFE. Furthermore, introduction of H atom causes bigger energy perturbation in the initial configuration, i.e., $E^{H}_{SF} - E_{SF} < E^{H}_{ini} - E_{ini}$, implying hydrogen reduces SFE due to $E^{H}_{SF} - E^{H}_{ini} < E_{SF} - E_{ini}$.

Here it is worth noting that these findings have revealed the mechanisms about a combined balance of opposing constraints such as

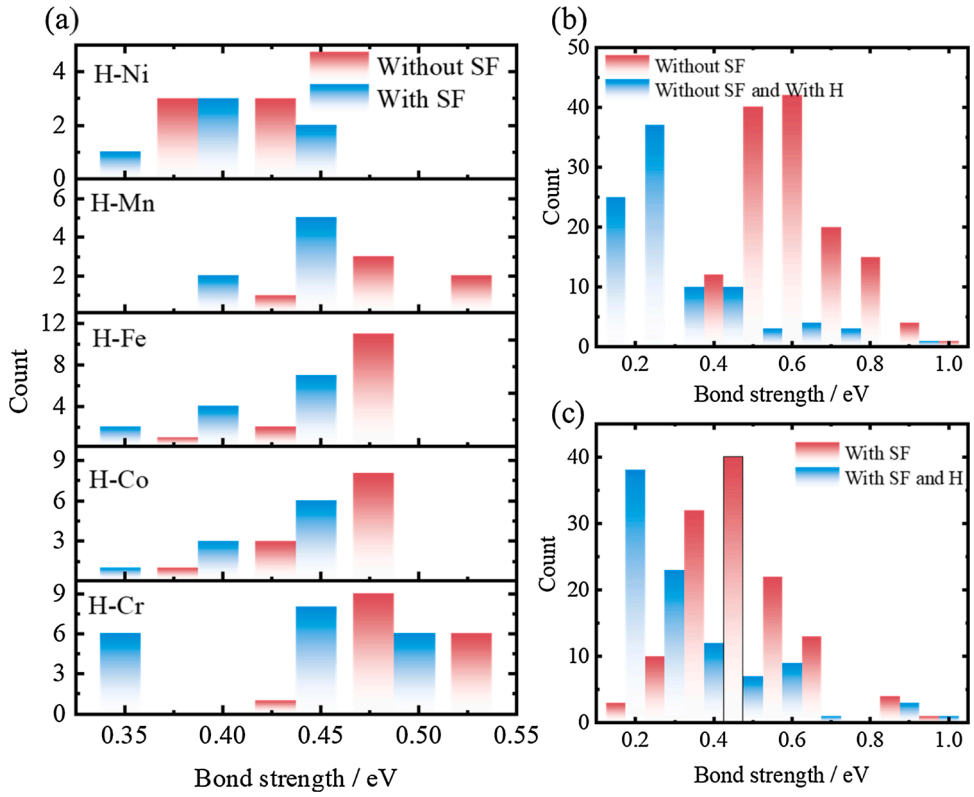

Fig. 8. (a) The bond strength statistics between H and metal atoms in configurations without SF and ones with SF. (b) Bond strength statistics between metal atoms in configurations without SF and ones without SF but with H. (c) Bond strength statistics between metal atoms in configurations with SF and ones with SF and H.

strength, ductility and hydrogen embrittlement in HEAs. There are two main influencing effects: (i) The solid solution elements lead to a low hydrogen diffusion coefficient, suppressing high local hydrogen accumulation, and (ii) the stacking fault energy of HEAs is reduced by hydrogen, promoting formation of nanotwins and enhancing local strain hardening. The interaction between hydrogen and defects in HEAs is quite distinct from that of other steels or intermetallics with low diffusion coefficients. For example, accumulation of hydrogen at defects in intermetallics results in hydrogen-enhanced decohesion [8,64] and formation of hydrogen bubble [65] or hydride [15], which accelerates, rather than decreases, damage and failure.

4. Conclusion

In summary, by using the first-principles method in combination with the special quasi-random structure technique, hydrogen embrittlement of HEAs have been investigated from the viewpoints of hydrogen solution and diffusion as well as the interaction between hydrogen and dislocations. In contrast to traditional alloys, the solution energy appears fluctuation due to different bond strengths of H and metal atoms. The high diffusion barrier leads to trapping of H in low energy sites. It is shown that hydrogen diffuses only along paths of OI–TI and TI–OI, and the distinct forward and backward vibration frequencies and diffusion barriers break periodicity and symmetry of hydrogen diffusion in HEAs. It leads to sluggish diffusion of hydrogen in HEAs and slows down aggregation of hydrogen. In hydrogen-free HEAs, SFE increases with local contents of Mn and Cr, and decreases with Co. Furthermore, introduction of H induces the transfer of charge from metal to H atoms, leading to the increase of metal-metal bond length and the decease of bond strength, which reduces stable and unstable SFE. These findings provide a theoretical basis for better understanding the excellent hydrogen embrittlement mechanism of HEAs.

Declaration of Competing Interest

The authors report no declarations of interest.

Acknowledgements

This work is financially supported by the National Natural Science Foundation of China (Nos. 11790292 and 11672299), the National Key Research and Development Program of China (No. 2017YFB0702003), the Strategic Priority Research Program (Nos. XDB22040302 and XDB22040303), the Key Research Program of Frontier Sciences (No. QYZDJSSW-JSC011), Science Challenge Project (No. TZ2016001), the Youth Promotion Association of Chinese Academy of Sciences (No. 2017025), and the opening project of State Key Laboratory of Explosion Science and Technology, Beijing Institute of Technology.

References

[1] W.H. Johnson, On some remarkable changes produced in iron and steel by the action of hydrogen and acids, Proc. R. Soc. Lond. 23 (1875) 168–179.
[2] Y.S. Chen, H. Lu, J. Liang, A. Rosenthal, H. Liu, G. Sneddon, I. McCarroll, Z. Zhao, W. Li, A. Guo, J.M. Cairney, Observation of hydrogen trapping at dislocations, grain boundaries, and precipitates, Science 367 (2020) 171–175.
[3] Y.-S. Chen, D. Haley, S.S.A. Gerstl, A.J. London, F. Sweeney, R.A. Wepf, W. M. Rainforth, P.A.J. Bagot, M.P. Moody, Direct observation of individual hydrogen atoms at trapping sites in a ferritic steel, Science 355 (2017) 1196–1199.
[4] J. Venezuela, Q. Zhou, Q. Liu, H. Li, M. Zhang, M.S. Dargusch, A. Atrens, The influence of microstructure on the hydrogen embrittlement susceptibility of martensitic advanced high strength steels, Mater. Today Commun. 17 (2018) 1–14.
[5] R.A. Oriani, A mechanistic theory of hydrogen embrittlement of steels, Ber. Bunsen. Ges. Phys. Chem. 76 (1972) 848–857.
[6] M.S. Daw, M.I. Baskes, Semiempirical, quantum mechanical calculation of hydrogen embrittlement in metals, Phys. Rev. Lett. 50 (1983) 1285.
[7] A. Tehranchi, X. Zhou, W.A. Curtin, A decohesion pathway for hydrogen embrittlement in nickel: mechanism and quantitative prediction, Acta Mater. 185 (2019) 98–109.

[8] J.W. Cohron, E.P. George, L. Heatherly, C.T. Liu, R.H. Zee, Effect of low-pressure hydrogen on the room-temperature tensile ductility and fracture behavior of Ni3Al, Intermetallics 4 (1996) 497–502.

[9] Y. Chen, Y.W. Chung, The role of hydrogen diffusion and desorption in moisture-induced embrittlement in intermetallics doped with alloying elements, Intermetallics 11 (2003) 551–554.

[10] I.M. Robertson, H.K. Birnbaum, An HVEM study of hydrogen effects on the deformation and fracture of nickel, Acta Metall. 34 (1986) 353–366.

[11] G. Lu, Q. Zhang, N. Kioussis, E. Kaxiras, Hydrogen-enhanced local plasticity in aluminum: an ab initio study, Phys. Rev. Lett. 87 (2001), 095501.

[12] I.H. Katzarov, D.L. Pashov, A.T. Paxton, Hydrogen embrittlement I. Analysis of hydrogen-enhanced localized plasticity: effect of hydrogen on the velocity of screw dislocations in α -Fe, Phys. Rev. Mater. 1 (2017), 033602.

[13] M. Koyama, S.M. Taheri-Mousavi, H. Yan, J. Kim, B.C. Cameron, S.S. Moeini-Ardakani, J. Li, C.C. Tasan, Origin of micrometer-scale dislocation motion during hydrogen desorption, Sci. Adv. 6 (2020) 1187.

[14] S. Takano, T. Suzuki, An electron-optical study of β-hydride and hydrogen embrittlement of vanadium, Acta Metall. 22 (1974) 265–274.

[15] L. Thuinet, R. Besson, Ab initio study of competitive hydride formation in zirconium alloys, Intermetallics. 20 (2012) 24–32.

[16] G. Lu, E. Kaxiras, Hydrogen embrittlement of aluminum: the crucial role of vacancies, Phys. Rev. Lett. 94 (2005), 155501.

[17] X.L. Ren, P.H. Shi, W.W. Zhang, X.Y. Wu, Q. Xu, Y.X. Wang, Swamps of hydrogen in equiatomic FeCuCrMnMo alloys: first-principles calculations, Acta Mater. 180 (2019) 189–198.

[18] H. Luo, S.S. Sohn, W. Lu, L. Li, X. Li, C.K. Soundararajan, W. Krieger, Z. Li, D. Raabe, A strong and ductile medium-entropy alloy resists hydrogen embrittlement and corrosion, Nat. Commun. 11 (2020) 3081.

[19] J.W. Yeh, S.K. Chen, S.J. Lin, J.Y. Gan, T.S. Chin, T.T. Shun, C.H. Tsau, S.Y. Chang, Nanostructured high-entropy alloys with multiple principal elements: novel alloy design concepts and outcomes, Adv. Eng. Mater. 6 (2004) 299–303.

[20] B. Cantor, I.T.H. Chang, P. Knight, A.J.B. Vincent, Microstructural development in equiatomic multicomponent alloys, Mater. Sci. Eng. A 375 (2004) 213–218.

[21] E.P. George, D. Raabe, R.O. Ritchie, High-entropy alloys, Nat. Rev. Mater. 4 (2019) 515–534.

[22] B. Gludovatz, A. Hohenwarter, D. Catoor, E.H. Chang, E.P. George, R.O. Ritchie, A fracture-resistant high-entropy alloy for cryogenic applications, Science 345 (2014) 1153–1158.

[23] Z. Lei, X. Liu, Y. Wu, H. Wang, S. Jiang, S. Wang, X. Hui, Y. Wu, B. Gault, P. Kontis, D. Raabe, L. Gu, Q. Zhang, H. Chen, H. Wang, J. Liu, K. An, Q. Zeng, T.G. Nieh, Z. Lu, Enhanced strength and ductility in a high-entropy alloy via ordered oxygen complexes, Nature 563 (2018) 546–550.

[24] Z. Li, K.G. Pradeep, Y. Deng, D. Raabe, C.C. Tasan, Metastable high-entropy dual-phase alloys overcome the strength-ductility trade-off, Nature 534 (2016) 227–230.

[25] Z. Fu, L. Jiang, J.L. Wardini, B.E. MacDonald, H. Wen, W. Xiong, D. Zhang, Y. Zhou, T.J. Rupert, W. Chen, E.J. Lavernia, A high-entropy alloy with hierarchical nanoprecipitates and ultrahigh strength, Sci. Adv. 4 (2018) 8712.

[26] Y. Bu, Z. Li, J. Liu, H. Wang, D. Raabe, W. Yang, Nonbasal slip systems enable a strong and ductile hexagonal-close-packed high-entropy phase, Phys. Rev. Lett. 122 (2019), 075502.

[27] Z. Li, S. Zhao, R.O. Ritchie, M.A. Meyers, Mechanical properties of high-entropy alloys with emphasis on face-centered cubic alloys, Prog. Mater. Sci. 102 (2019) 296–345.

[28] J.P. Liu, J.X. Chen, T.W. Liu, C. Li, Y. Chen, L.H. Dai, Superior strength-ductility CoCrNi medium-entropy alloy wire, Scr. Mater. 181 (2020) 19–24.

[29] Z. Fu, B.E. MacDonald, A.D. Dupuy, X. Wang, T.C. Monson, R.E. Delaney, C. J. Pearce, K. Hu, Z. Jiang, Y. Zhou, J.M. Schoenung, W. Chen, E.J. Lavernia, Exceptional combination of soft magnetic and mechanical properties in a heterostructured high-entropy composite, Appl. Mater. Today 15 (2019) 590–598.

[30] W. Huo, H. Zhou, F. Fang, X. Zhou, Z. Xie, J. Jiang, Microstructure and properties of novel CoCrFeNiTax eutectic high-entropy alloys, J. Alloys Compd. 735 (2018) 897–904.

[31] Z.J. Jiang, J.Y. He, H.Y. Wang, H.S. Zhang, Z.P. Lu, L.H. Dai, Shock compression response of high entropy alloys, Mater. Res. Lett. 4 (2016) 226–232.

[32] X.F. Liu, T. Zhili, X.F. Zhang, H.H. Chen, L.H. Dai, Self-sharpening" tungsten high-entropy alloy, Acta Mater. 186 (2020) 257–266.

[33] Z. Li, S. Zhao, S.M. Alotaibi, Y. Liu, M.A. Meyers, Adiabatic shear localization in the CrMnFeCoNi high-entropy alloy, Acta Mater. 151 (2018) 424–431.

[34] J. Ding, Q. Yu, M. Asta, R.O. Ritchie, Tunable stacking fault energies by tailoring local chemical order in CrCoNi medium-entropy alloys, Proc. Natl. Acad. Sci. 115 (2018) 8919–8924.

[35] Q.J. Li, H. Sheng, E. Ma, Strengthening in multi-principal element alloys with local-chemical-order roughened dislocation pathways, Nat. Commun. 10 (2019) 3563.

[36] Y.H. Zhang, Y. Zhuang, A. Hu, J.J. Kai, C.T. Liu, The origin of negative stacking fault energies and nano-twin formation in face-centered cubic high entropy alloys, Scr. Mater. 130 (2017) 96–99.

[37] S. Liu, Y. Wei, The Gaussian distribution of lattice size and atomic level heterogeneity in high entropy alloys, Extrem. Mech. Lett. 11 (2017) 84–88.

[38] Q. Ding, Y. Zhang, X. Chen, X. Fu, D. Chen, S. Chen, L. Gu, F. Wei, H. Bei, Y. Gao, M. Wen, J. Li, Z. Zhang, T. Zhu, R.O. Ritchie, Q. Yu, Tuning element distribution, structure and properties by composition in high-entropy alloys, Nature 574 (2019) 223–227.

[39] B.E. MacDonald, Z. Fu, X. Wang, Z. Li, W. Chen, Y. Zhou, D. Raabe, J. Schoenung, H. Hahn, E.J. Lavernia, Influence of phase decomposition on mechanical behavior of an equiatomic CoCuFeMnNi high entropy alloy, Acta Mater. 181 (2019) 25–35.

[40] F.X. Zhang, S. Zhao, K. Jin, H. Xue, G. Velisa, H. Bei, R. Huang, J.Y.P. Ko, D. C. Pagan, J.C. Neuefeind, W.J. Weber, Y. Zhang, Local structure and short-range order in a NiCoCr solid solution alloy, Phys. Rev. Lett. 118 (2017), 205501.

[41] L. Li, R.D. Kamachali, Z. Li, Z. Zhang, Grain boundary energy effect on grain boundary segregation in an equiatomic high-entropy alloy, Phys. Rev. Mater. 4 (2020), 053603.

[42] K. Ming, L. Li, Z. Li, X. Bi, J. Wang, Grain boundary decohesion by nanoclustering Ni and Cr separately in CrMnFeCoNi high-entropy alloys, Sci. Adv. 5 (2019) 1–8.

[43] G. Yang, Y. Zhao, D.H. Lee, J.M. Park, M.Y. Seok, J.Y. Suh, U. Ramamurty, J. il Jang, Influence of hydrogen on incipient plasticity in CoCrFeMnNi high-entropy alloy, Scr. Mater. 161 (2019) 23–27.

[44] Y. Zhao, D.H. Lee, J.A. Lee, W.J. Kim, H.N. Han, U. Ramamurty, J.Y. Suh, J. Jang, Hydrogen-induced nanohardness variations in a CoCrFeMnNi high-entropy alloy, Int. J. Hydrogen Energy 42 (2017) 12015–12021.

[45] Z. Pu, Y. Chen, L.H. Dai, Strong resistance to hydrogen embrittlement of high-entropy alloy, Mater. Sci. Eng. A 736 (2018) 156–166.

[46] Y. Zhao, J.M. Park, D.H. Lee, E.J. Song, J.Y. Suh, U. Ramamurty, J. il Jang, Influences of hydrogen charging method on the hydrogen distribution and nanomechanical properties of face-centered cubic high-entropy alloy: a comparative study, Scr. Mater. 168 (2019) 76–80.

[47] Y. Zhao, D.H. Lee, M.Y. Seok, J.A. Lee, M.P. Phaniraj, J.Y. Suh, H.Y. Ha, J.Y. Kim, U. Ramamurty, J. Jang, Resistance of CoCrFeMnNi high-entropy alloy to gaseous hydrogen embrittlement, Scr. Mater. 135 (2017) 54–58.

[48] H. Luo, Z. Li, D. Raabe, Hydrogen enhances strength and ductility of an equiatomic high-entropy alloy, Sci. Rep. 7 (2017) 1–7.

[49] H. Luo, W. Lu, X. Fang, D. Ponge, Z. Li, D. Raabe, Beating hydrogen with its own weapon: nano-twin gradients enhance embrittlement resistance of a high-entropy alloy, Mater. Today 21 (2018) 1003–1009.

[50] X. Lu, D. Wang, Z. Li, Y. Deng, A. Barnoush, Hydrogen susceptibility of an interstitial equimolar high-entropy alloy revealed by in-situ electrochemical microcantilever bending test, Mater. Sci. Eng. A 762 (2019) 138114.

[51] Y.J. Kwon, J.W. Won, S.H. Park, J.H. Lee, K.R. Lim, Y.S. Na, C.S. Lee, Ultrahigh-strength CoCrFeMnNi high-entropy alloy wire rod with excellent resistance to hydrogen embrittlement, Mater. Sci. Eng. A 732 (2018) 105–111.

[52] Y. Zhao, D.H. Lee, W.J. Kim, M.Y. Seok, J.Y. Kim, H.N. Han, J.Y. Suh, U. Ramamurty, J. Jang, Influence of pre-strain on the gaseous hydrogen embrittlement resistance of a high-entropy alloy, Mater. Sci. Eng. A 718 (2018) 43–47.

[53] K.E. Nygren, K.M. Bertsch, S. Wang, H. Bei, A. Nagao, I.M. Robertson, Hydrogen embrittlement in compositionally complex FeNiCoCrMn FCC solid solution alloy, Curr. Opin. Solid State Mater. Sci. 22 (2018) 1–7.

[54] Q. Ding, Y. Zhang, X. Chen, X. Fu, D. Chen, S. Chen, L. Gu, F. Wei, H. Bei, Y. Gao, M. Wen, J. Li, Z. Zhang, T. Zhu, R.O. Ritchie, Q. Yu, Tuning element distribution, structure and properties by composition in high-entropy alloys, Nature 574 (2019) 223–227.

[55] T. Luo, Y. Peng, Y. Guo, J. Cao, Influence of interactions between hydrogen and (1012) twin boundary on hydrogen embrittlement in α-Ti, Mater. Today Commun. (2020), 101802.

[56] G. Kresse, J. Furthmüller, Efficiency of ab-initio total energy calculations for metals and semiconductors using a plane-wave basis set, Comput. Mater. Sci. 6 (1996) 15–50.

[57] A. Zunger, S.H. Wei, L.G. Ferreira, J.E. Bernard, Special quasirandom structures, Phys. Rev. Lett. 65 (1990) 353–356.

[58] D. Sheppard, P. Xiao, W. Chemelewski, D.D. Johnson, G. Henkelman, A generalized solid-state nudged elastic band method, J. Chem. Phys. 136 (2012), 074103.

[59] M. Mantina, Y. Wang, L.Q. Chen, Z.K. Liu, C. Wolverton, First principles impurity diffusion coefficients, Acta Mater. 57 (2009) 4102–4108.

[60] R.J. Asaro, S. Suresh, Mechanistic models for the activation volume and rate sensitivity in metals with nanocrystalline grains and nano-scale twins, Acta Mater. 53 (2005) 3369–3382.

[63] R. Nelson, C. Ertural, J. George, V.L. Deringer, G. Hautier, R. Dronskowski, LOBSTER : local orbital projections, atomic charges, and chemical-bonding analysis from projector-augmented-wave-based density-functional theory, J. Comput. Chem. (2020) 26353.

[64] C.T. Liu, E.P. George, Intermetallics: environmental embrittlement. Encycl. Mater. Sci. Technol, Elsevier, 2001, pp. 4181–4186.

[65] V. Shankar Rao, Some observations on the hydrogen embrittlement of Fe_3Al-Fe_3AlC intermetallic compounds, Mater. Res. Bull. 39 (2004) 169–174.